Nanoscale

ARTICLE

Simultaneous Topographical, Electrical and Optical Microscopy of Optoelectronic Devices at the Nanoscale

Naresh Kumar, [a]* Alina Zoladek-Lemanczyk, [a] Anne A. Y. Guilbert, [b] Weitao Su [c], Sachetan M. Tuladhar, [b] Thomas Kirchartz, [b, d, e] Bob C. Schroeder, [f] Iain McCulloch, [f, g] Jenny Nelson, [b] Debdulal Roy [a] and Fernando A. Castro [a]*

Novel optoelectronic devices rely on complex nanomaterial systems where nanoscale morphology and local chemical composition are critical to performance. However, lack of analytical techniques that can directly probe these structure-property relationships at the nanoscale presents a major obstacle to device development. In this work, we present a novel method for non-destructive, simultaneous mapping of morphology, chemical composition and photoelectrical properties with < 20 nm spatial resolution by combining plasmonic optical signal enhancement with electrical-mode scanning probe microscopy. We demonstrate that this combined approach offers subsurface sensitivity that can be exploited to provide moleculer information with a nanoscale resolution in all three spatial dimensions. Applying the technique to an organic solar cell device, we show that the inferred surface and subsurface composition distribution correlates strongly with the local photocurrent generation and explains macroscopic device performance. For instance, direct measurement of fullerene phase purity can distinguish between high purity aggregates that lead to poor performance and lower purity aggregates (fullerene intercalated with polymer) that result in strong photocurrent generation and collection. We show that reliable determination of structure-property relationship at the nanoscale can remove ambiguity from macroscopic device data and support identification of the best routes for device optimisation. The multi-parameter measurement approach demonstrated here is expected to play a significant role in guiding the rational design of nanomaterial-based optoelectronic devices, by opening a new realm of possibilities for advanced investigation via combination of nanoscale optical spectroscopy with a whole range of scanning probe microscopy modes.

1. Introduction

Understanding the pivotal role of nanoscale properties in defining the performance of electronic and optoelectronic devices has led to new opportunities for materials applications[1-3] and a push towards the development of new measurement techniques that can probe different device properties at increasing spatial resolution[2, 4]. However, despite a significant progress in the development of

a. National Physical Laboratory, Teddington, Middlesex, U.K. TW11 0LW
b. Department of Physics, Imperial College London, London, U.K. SW7 2AZ
c. Institute of Materials Physics, Hangzou Dianzi University, 310018 Hangzou, China
d. IEK-5 Photovoltaik, Forschungzentrum Juelich 52425, Germany
e. Faculty of Engineering and CENIDE, University of Duisburg-Essen,9 Carl-Benz-Strasse 199, 47057 Duisburg, Germany
f. Department of Chemistry, Imperial College London, London, U.K. SW7 2AZ, 6SPERC
g. King Abdullah University of Science and Technology (KAUST), Thuwal, 23955-6900, Saudi Arabia
*Email: naresh.kumar@npl.co.uk, fernando.castro@npl.co.uk

nanoscale characterisation techniques, existing analytical techniques can only measure either electrical or spectroscopic properties, but not both simultaneously. Additionally, high-resolution information is rarely obtained simultaneously in all three dimensions[4]. For instance, in photoconductive (PC) − atomic force microscopy (AFM) a metal-coated AFM tip in contact with the active layer acts as a nano-electrical probe to measure the photocurrent generated, when the solar cell is excited by a light source. PC-AFM can be used to probe the optoelectronic properties of operating organic solar cells correlating topography and photovoltaic performance with a lateral resolution of 20 - 50 nm[5-7]; however, it does not provide direct information about the chemical composition of the active layer. On the other hand, tip-enhanced optical spectroscopy (TEOS)[8] is a powerful and reliable[9] technique that allows simultaneous mapping of the chemical composition (via Raman and photoluminescence (PL) signals) and topography of a surface at the nanoscale. In TEOS, localised surface plasmon (LSP) resonance excited at a metal-coated tip enhances and confines the electromagnetic field (also called "near-field") to an area similar to the size of the tip-apex providing a typical spatial resolution of < 25 nm in the Raman and PL maps, which is about ten times better than the diffraction-limited lateral resolution (200 − 300 nm) of a confocal optical microscope[10]. TEOS has been successfully applied for surface characterisation

in a wide range of research areas including catalysis[11, 12], semiconductors[13], OPV devices[14], graphene[15-17], single-layer molybdenum disulphide (MoS_2)[18, 19], biology[20] and single molecule imaging[21]. However, simultaneous high-resolution electrical information cannot be obtained using TEOS.

In this work, we demonstrate a novel method for simultaneous characterisation of topography, chemical composition and photoelectrical properties of a surface with nanoscale resolution both vertically and laterally by integrating TEOS and PC-AFM into a single measurement. This unique approach also solves the crucial issue of finding the exact same location when performing a sequence of experiments on a sample, which is not only very challenging but can also lead to unwanted contamination and/or degradation when samples are moved from one instrument to another. Furthermore, this method allows charaterisation of optoelectronic devices under operating conditions. As a proof of principle, we apply this method to model polymer:fullerene blend solar cells and demonstrate that it can identify a hierarchical 3D nanostructure and directly correlate local composition to photocurrent generation and collection, including the identification of impurity within nanoscopic phase domains and the direct correlation of nanoscale properties to macroscopic device performance. Finally, we highlight the potential of this novel methodology for the investigation of other nanomaterials and nanoscale devices.

Recent years have seen a steep rise in the efficiency of organic photovoltaic (OPV) devices, due in part to the growing appreciation of the active layer nanomorphology in determining device performance[22, 23]. An OPV device typically consists of two electrodes sandwiching an active layer, which is blend of a conjugated polymer acting as electron donor (D) and a fullerene derivative acting as electron acceptor (A). Light absorption generates bound excitons in OPV devices that need to be dissociated into free charge carriers at a D-A heterojunction for photocurrent generation. Short exciton diffusion lengths within organic semiconductors necessitate optimisation of domain structure within the D-A blend films for efficient charge generation whilst maintaining well-connected pathways within each material type for efficient charge collection[22]. Therefore, D-A blends with coarse phase-separated morphologies (> 100 nm) typically yield a low device efficiency due to poor charge generation[24, 25] whilst blends with too intimate phase mixing yield worsened device performance due to poor charge collection or rapid exciton recombination[26]. Furthermore, it has been demonstrated that local microstructure and hence the device performance in OPV devices is a function of material choice[27], D-A blend ratio[28, 29] and process route[30]. Whilst surface imaging techniques such as atomic force microscopy (AFM) have been used to correlate the performance of solar cells with the apparent size of the observed phase-separated domains[31, 32], the rationale to relate domain size to device performance is neither consistent nor well understood. Part of the uncertainty results from the phase-separated domains often being impure in composition; in fact, several reports indicate that pure domains may be rare in polymer-fullerene blends[27, 33, 34]. Additionally, it is known that the polymer:fullerene ratio may
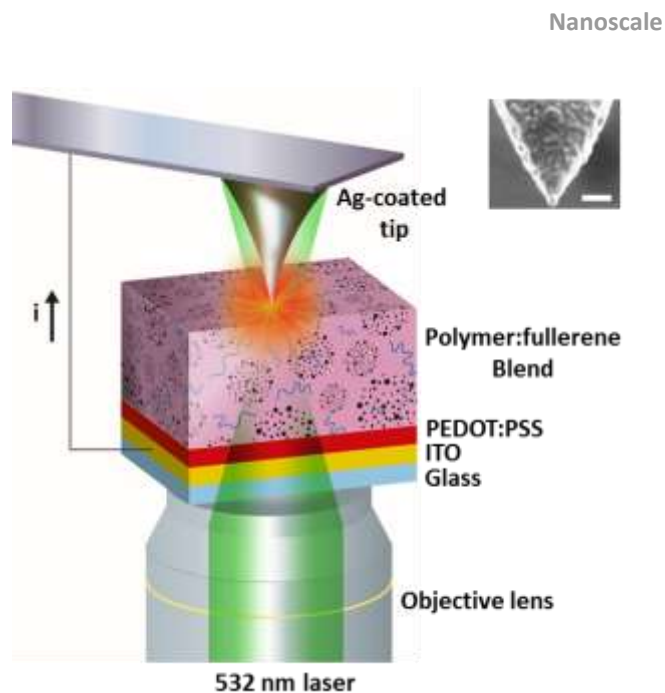

Fig. 1   Schematic diagram of the solar cell device and experimental set-up used in this work.   A scanning electron microscope (SEM) image of a representative Ag-coated tip is shown in the inset. Scale bar: 200 nm. The radius of the tip-apex is ≈25 nm.

vary laterally within blend films leading to mesoscale variations in photocurrent generation and collection, further complicating the relationship between average blend ratio and device performance[35].

In this work, we demonstrate that the proposed novel methodology that we refer to as "simultaneous topography, electrical and optical microscopy" (STEOM) allows simultaneous characterisation of topographical, electrical and optical spectroscopic properties providing a detailed understanding of the complex interplay of local morphology, chemical composition, and photocurrent generation in OPV devices at the nanoscale.

2.   Experimental details

2.1.   Experimental set-up

Schematic diagram of the solar cell device and experimental set-up used in this work is presented in Fig. 1. (see Supplementary Fig. S1 for a more detailed schematic diagram of the optical set-up). A home-built TEOS system in transmission mode consisting of an inverted confocal optical microscope (Nikon, Japan) fitted with an AFM (AIST-NT, USA) on top was used in this work. A Raman spectrometer (Horiba Scientific, UK) attached with an electron-multiplying charged coupled device detector (Andor Technology, Ireland) having quantum efficiency > 50% from 400 − 900 nm was used to measure the optical spectra. A radially polarised (ARCoptix, Switzerland) laser beam of wavelength 532 nm was focused onto the sample using a 100×, 1.49 NA oil-immersion objective lens (Nikon,

Japan). A relatively low laser power of 10 µW at the sample was used for all measurements to avoid thermal degradation of the sample. Fine alignment of Ag-coated tip and the laser spot was carried out using an XYZ piezoelectric scanner attached to the objective lens and all near-field measurements were performed using contact-mode AFM. The solar-cell samples were found to degrade rapidly during STEOM measurements under ambient conditions. Therefore, to avoid sample degradation and maintain plasmonic enhancement of the Ag-coated probe[36], all STEOM measurements were conducted inside a nitrogen environment. The nitrogen environment was set-up by placing a perspex box around the sample and AFM part of the system as shown in Supplementary Fig. S1. The air inside the box was purged out with a high nitrogen flow first till the oxygen concentration fell below 0.1%. Thereafter, a gentle flow of fresh nitrogen gas was used to maintain the oxygen concentration at that level.

2.2. Probe preparation

STEOM probes were prepared by first oxidising contact-mode Si AFM tips (Mikromasch, Estonia) to a thickness of 300 nm SiO_2 followed by thermal coating with Ag to a nominal thickness of 150 nm under 10^{-6} mbar pressure at a slow deposition rate of 0.05 nm/s. A thicker Ag coating of 150 nm was used for the probes compared to the typical thickness of 50 – 100 nm commonly used for preparing TEOS probes to ensure sufficient conductivity for PC-AFM measurements. Despite the 150 nm deposited nominal thickness, a typical radius of 25 nm was obtained at the conical tip-apex as shown in the SEM image of a representative STEOM tip in the inset of Fig. 1.

2.3. Sample preparation

Solar cell devices were prepared by first spin-coating filtered poly(3,4-ethylenedioxythiophene):poly(styrenesulfonate) (PEDOT: PSS) (Clevios AI 4083, Germany) aqueous solution onto indium tin oxide (ITO)-coated glass coverslips (Praezisions Glas & Optik GmbH, Germany) at 3500 revolutions per minute (RPM) for 60 s and annealed in air at 1500° C for 20 minutes. Then, 20 mg/ml solution of Poly[(2,1,3-benzothiadiazole-4,7-diyl)-*alt*-(4,9-dihydro-4,4,9,9-tetraoctylbenzo [1'',2'':4,5;4'',5'':4',5']bissilolo[3,2-*b*:3',2'-*b*']dithiophene-2,7-diyl)] (C8SiIDT-BT) (Synthesised at Imperial College London, UK) and 1',4'-Dihydro-naphtho[2',3':1,2][5,6]fullerene-C_{60} (ICMA) (Plextronics Inc., USA) (Weight ratio 1:1) in chlorobenzene was spin-coated on top of the PEDOT: PSS layer at 4000 RPM for 120 s followed by 5000 RPM for 60 s. Molecular structures of C8SiIDT-BT and ICMA molecules are shown in Fig. 2a. During the STEOM measurements, the Ag-coated tip acted as cathode (top electrode) for the solar cell device. However, for the macroscopic characterisation, the top electrode consisted of 20 nm calcium and 100 nm aluminium films deposited on top of solar cell blends by thermal evaporation under 10^{-6} mbar pressure. Current density–voltage (J–V) characteristics of the devices were measured using Keithley 236
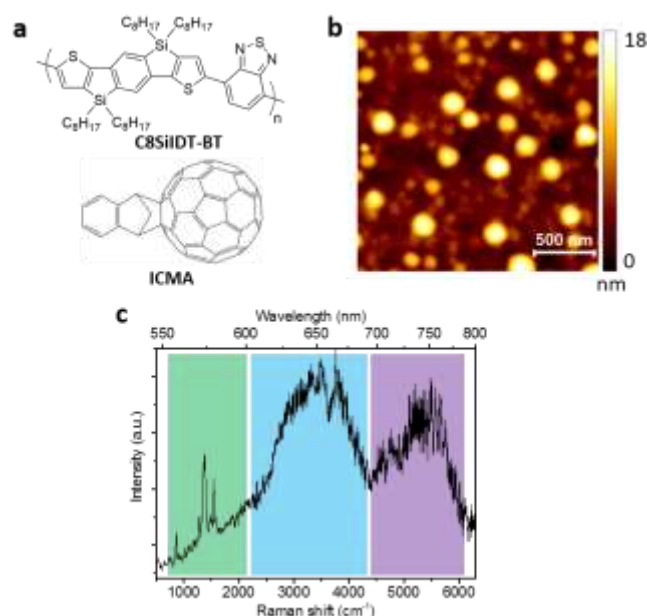

Fig. 2   (a) Molecular structures of C8SiIDT-BT and ICMA molecules. (b) Topography image of the C8SiIDT-BT:ICMA blend measured using tapping-mode AFM. (c) Confocal optical spectrum of the blend. Integration time: 1 s. The Raman and PL bands from C8SiIDT-BT and ICMA are highlighted.

Source Measure Unit (Tektronix Inc., USA). Performance of the solar cell devices was measured under 100 mW/cm² excitation by solar simulator (xenon lamp with AM1.5G filters).

3.   Results and discussion

In this work, a Ag-coated AFM tip placed in the laser focus and in contact with the solar cell active layer surface has been used to perform the dual function of a plasmonic probe for TEOS measurements and a cathode for PC-AFM measurements as schematically shown in Fig. 1. Under 532 nm laser illumination, photogenerated excitons dissociate at the polymer:fullerene interfaces in the solar cell active layer yielding electrons and holes that can be collected by the Ag-coated tip and the indium tin oxide (ITO) anode layer, respectively. Furthermore, LSP resonance of the tip-apex with 532 nm laser excitation leads to the enhancement of PL and Raman signals from the sample, thus enabling simultaneous topographic, chemical (via Raman signals), optical (via PL signals) and electrical mapping of the solar cell device with a nanoscale resolution. To demonstrate the feasibility of this multiparameter measurement method C8SiIDT-BT:ICMA blend solar cell device was chosen as a model system due to the presence of large resolvable domains in the active layer[37], despite which the solar cell device delivered a useful photocurrent of ≈2.8 mA/cm². See Supplementary Note 1 for details about the macroscopic characteristics and performance of C8SiIDT-BT:ICMA solar cell devices and their comparison with the macroscopic performance of pristine and annealed C8SiIDT-BT :[6,6]-phenyl-C61 butyric acid methyl ester ($PC_{61}BM$)
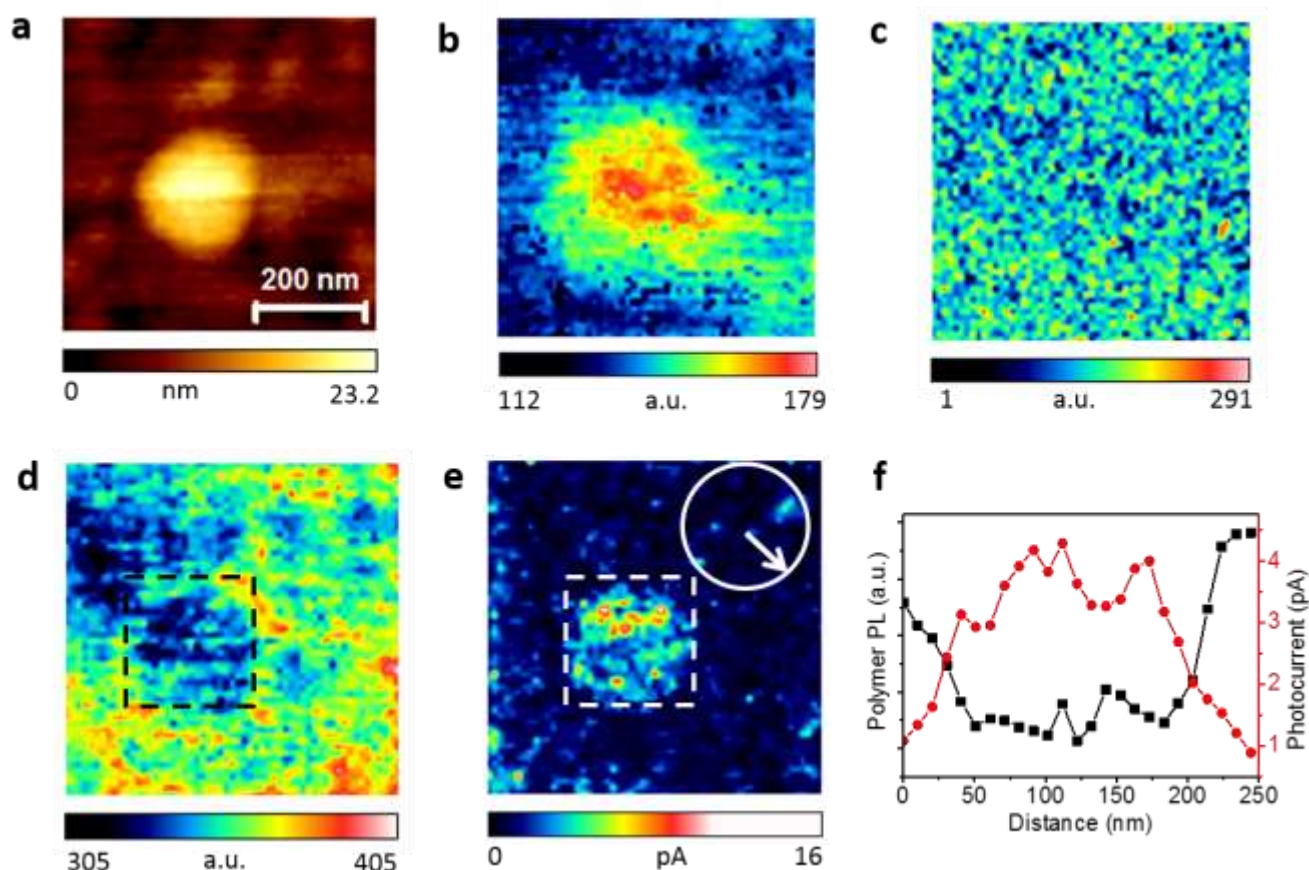
Fig. 3 High-resolution maps of (a) topography, (b) fullerene PL signal intensity (5400 cm^{-1} (746 nm)), (c) polymer Raman signal intensity (1382 cm^{-1}), (d) polymer PL signal intensity (3800 cm^{-1} (667 nm), and (e) photocurrent measured simultaneously from a 570 × 570 nm^2 area (57 × 57 pixels) around a topographic island on the C8SiIDT-BT:ICMA solar cell device. Spectrum integration time: 0.5 s. (f) Polymer PL (black) and photocurrent (red) intensity profiles averaged over the areas (going from right to left) marked by dashed squares in d and e. Lateral resolution of the optical spectroscopy and photocurrent maps is estimated to be < 20 nm. See Supplementary Note 3 for details about the estimation of spatial resolution.

solar cell devices. Topographical domains of 50 - 250 nm can be clearly seen in the AFM topography image of C8SiIDT-BT:ICMA (hereafter also referred to as "polymer:fullerene") blend film shown in Fig. 2b. The non-uniform character of these C8SiIDT-BT blends with ICMA, in contrast to PC$_{61}$BM (see the topography image in Supplementary Fig. S3), allows us to probe multiple compositions in a single device and hence directly correlate local chemical composition with photocurrent generation efficiency. Confocal optical spectrum of the C8SiIDT-BT:ICMA blend shown in Fig. 2c consists of three spectrally well-separated bands, containing Raman bands from the polymer molecules and PL bands from both polymer and fullerene molecules, which are highlighted in Fig. 2c in different colours. The green region contains Raman bands from the polymer at 864 cm^{-1}, 1279 cm^{-1}, 1356 cm^{-1}, 1382 cm^{-1} and 1545 cm^{-1}, blue region contains the broad PL band from polymer at 3800 cm^{-1} (667 nm, 1.86 eV) and the purple region contains the PL band from fullerene at 5400 cm^{-1} (746 nm, 1.66 eV). The Raman band of ICMA at 1467 cm^{-1} is too weak to be distinguished from noise in the optical spectrum.

3.1. Simultaneous topography, electrical and optical microscopy

Prior to conducting STEOM measurements, plasmonic signal enhancement of Ag-coated probes was optimised by measuring optical enhancement factor of different Ag-coated tips on pristine C8SiIDT-BT and ICMA films. A significant improvement in the plasmonic enhancement of optical signals was obtained when Si AFM tips were oxidised to 300 nm thick SiO$_2$ in a tube furnace before deposition of Ag. See supplementary Note 2 for a discussion of the plasmonic enhancement of optical signals from pristine C8SiIDT-BT and ICMA films using a representative plasmonically active Ag-coated tip. Only the probes showing high plasmonic enhancement of optical signals were used for the mapping of C8SiIDT-BT:ICMA solar cell device. High-resolution maps of topography, fullerene PL signal intensity, polymer Raman signal intensity, polymer PL signal intensity and photocurrent around a topographic island on the C8SiIDT-BT:ICMA photoactive layer are shown in Fig. 3a - 3e, respectively. Here, the polymer Raman signal is used to map the distribution of polymer content on the blend surface, since the intensity of Raman peaks is proportional to the number of

scatterers in the probed volume. The intensity of polymer PL and fullerene PL depends on the local composition as well as the local degree of mixing of the two components (due to exciton quenching near the D-A interface). Therefore, the comparison of Raman and PL signal intensities allows us to probe the degree of polymer/fullerene mixing independently of the relative local polymer content [38, 39].

An important aspect of this work is the realisation that tip-enhanced PL (TEPL) and tip-enhanced Raman (TER) probe depths inside a sample are different and therefore could allow us to obtain vertically resolved information at the surface using combined data analysis. Here, probe depth is defined as the depth within the sample at which the measured signal intensity drops to $1/e$ times the intensity at the surface. The probe depths for TER and TEPL signals can be determined by the dependence of TER ($\propto E^4$) and TEPL ($\propto E^2\eta$) signal intensities on the electric field enhancement (E), where η is the PL quantum efficiency in the near-field that can be different from that in the far-field[40] and E is the ratio of electric field amplitude in the near-field to the far-field. In the near-field, both Raman and PL signals are amplified ($\propto E^2$) due to the interaction of the localised surface plasmon (LSP) of the tip with the incoming laser beam. However, for sufficiently small Raman shifts, the tip will also enhance the Raman emission signal with the same factor ($\propto E^2$) leading to an overall E^4 proportionality for TER signals. In the case of TEPL signals, the difference of the emission and
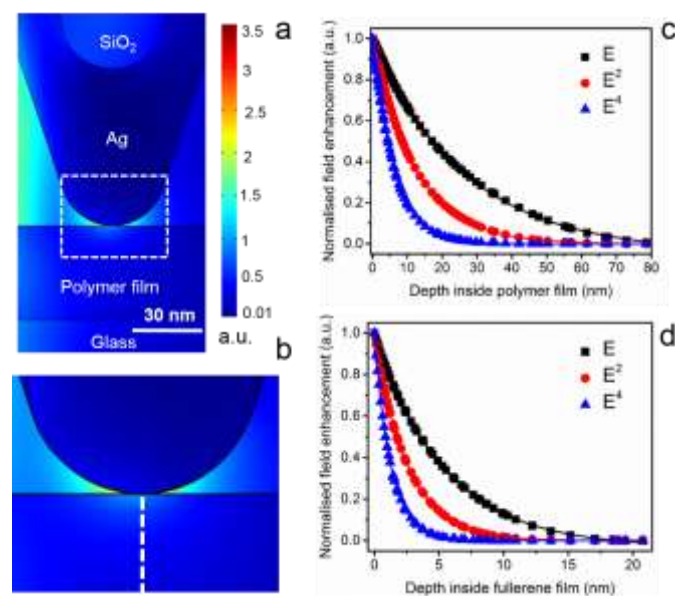
Fig. 4 (a) Numerical simulation map of the near-field intensity at the apex of a Ag-coated tip in pristine polymer film. (b) Zoomed-in simulated map of the intensity of near-field in the region marked by dashed rectangle in (a). (c) Plots of normalised E, E^2 and E^4 intensities within the pristine polymer film measured along the dashed line marked in (b). Plots are fitted with an exponential function shown in solid black, red and blue curves. (d) Plots of normalised E, E^2 and E^4 intensities within a pristine fullerene film fitted with exponential function shown as solid curves.

Table 1. Summary of near-field decay length, and probe depths of Raman and PL signals in pristine polymer and fullerene films calculated from the numerical simulation results shown in Fig. 4.

	Near-field decay length (nm) (E)	TEPL probe depth (nm) (E^2)	TER probe depth (nm) (E^4)
Polymer	26.4	12.3	6.1
Fullerene	5.4	2.6	1.3

excitation wavelengths are much larger compared to TER signals. Therefore, due to the finite energetic width of the LSP, the amplification of the PL quantum yield η in the near-field is much lower than the enhancement of the Raman signals as shown in Supplementary Note 4 for the samples used in this work.

To support our reasoning and investigate the probe depth of TER and TEPL signals within our samples, we carried out numerical simulations of electric field enhancement at the apex of a Ag-coated tip at the surface of pristine polymer and fullerene films using a commercial finite-element method solver (Comsol Multiphysics®). For the simulations, the geometry of the Ag-coated tip was kept similar to the ones used in this work along with the optical constants of the polymer and fullerene films. See Supplementary Note 5 for further details of the simulation parameters. Numerical simulation results are presented in Fig. 4. Fig. 4a shows the map of electric field intensity at the apex of a Ag-coated tip in contact with the polymer film. A zoomed-in map of the near-field intensity at the point of contact of the tip with the sample is shown in Fig. 4b. Highest near-field intensity is observed at the tip-apex, which decreases with increasing distance from the tip-apex within the sample. The normalised field enhancement (E) measured along the dashed line marked in Fig. 4b is plotted as black squares in Fig 4c. The decay length of the near-field within the polymer can be calculated by fitting an exponential curve to this plot to be 26.4 nm. Since TER and TEPL signal intensities are $\propto E^4$ and $\propto E^2$, respectively, the probe depth of TER and TEPL signal within the pristine polymer film can be estimated from the plots E^2 and E^4 in Fig. 4c to be 12.3 nm and 6.1 nm, respectively. Plots of normalised E, E^2 and E^4 intensities within a pristine fullerene film along with the fitted exponential functions are shown in Fig. 4d. The decay length of near-field and probe depths of TER and TEPL signals within the pristine fullerene film are estimated to be 5.4 nm, 2.6 nm and 1.3 nm, respectively. These simulation results are summarised in Table 1. The calculated probe depth of TER signals in pristine polymer and fullerene films is similar to the previous experimental reports of the decay length of TER signals measured using single-wall carbon nanotube samples[41, 42].

In Fig. 3, the STEOM maps show that within the topographic island region (Fig. 3a), the intensity of fullerene PL (Fig. 3b) and photocurrent under short-circuit conditions (Fig. 3e) increase, while the intensity of polymer PL is reduced (Fig. 3d), relative to the region outside the islands. An inverse correlation between macroscopic polymer PL intensity and photocurrent is often observed in OPVs and assigned to the increased photocurrent

generation via increased intermixing between donor and acceptor phases. Within these nanoscale measurements, we also observe an inverse correlation between polymer PL emission and photocurrent as shown in Fig. 3f (more details in Supplementary Note 6), however an explanation based on increased blend intermixing fails to explain the increase in fullerene PL emission. A higher fullerene PL emission in polymer blends has previously been assigned to the presence of large fullerene aggregates[38, 39]. Fig. 3c shows that the distribution of polymer Raman intensity is equally uniform both inside and outside the island. Since the probe depth of TEPL signals in fullerene (2.6 nm) is smaller than the probe depth of TER signal in the polymer (6.1 nm) as calculated using numerical simulations (Table 1), this indicates that a homogenous distribution of polymer molecules should exist near the very top surface (< 2.6 nm) of the sample. Furthermore, a comparison of fullerene TEPL map in Fig. 3b, polymer TEPL map in Fig. 3d and polymer TER map in Fig. 3c suggests a decreased relative polymer-to-fullerene composition at the subsurface. This indicates that the fullerene molecules aggregate at the subsurface leading to topographical features whereas the top surface consists of a uniform matrix, likely a fine mixture of polymer and fullerene molecules. This signifies that in this blend the fullerene aggregation is beneficial for efficient charge collection leading to higher photocurrent in those regions. Furthermore, the nanoscale pockets of higher photocurrent inside the islands shown in Fig. 3e indicate that these fullerene aggregates are not pure in composition but consist of a finer structure not visible from topography measurements. Indeed if these were pure fullerene aggregates the local photocurrent would decrease, as observed with STEOM measurements of relatively pure $PC_{61}BM$ aggregates within annealed $C8SiIDT-BT:PC_{61}BM$ solar cell blend as shown in Supplementary Note 7. Polymer molecules must be present around the subsurface fullerene aggregates for efficient charge separation at the polymer:fullerene interfaces leading to the observed pockets of high photocurrent in Fig. 3e.

3.2. Photocurrent and spectroscopic analysis outside the island

Similar to the nanoscale pockets of large photocurrent inside the islands, we also notice very small areas with large photocurrent outside the island, which we refer to as "current hotspots". Care needs to be taken when interpreting nanoscale variation in PC-AFM measurements as these can be caused by experimental artefacts and random current fluctuations[7] even in nominally homogeneous samples. Herein, we show that the combination of photocurrent with spectroscopic data is a powerful method to confirm that such variations are real and significant. Fig. 5 shows average (per pixel) photocurrent (Fig. 5a) and intensity of polymer Raman (red squares), polymer PL (green circles) and fullerene PL (blue triangles) signals (Fig. 5b) calculated in circular areas inside the white circle marked in Fig. 3e, as a function of radius increasing from 10 - 150 nm in the direction of the arrow. As the radius of the circular probe area increases, the average polymer Raman signal remains roughly constant, indicating a uniform distribution of polymer
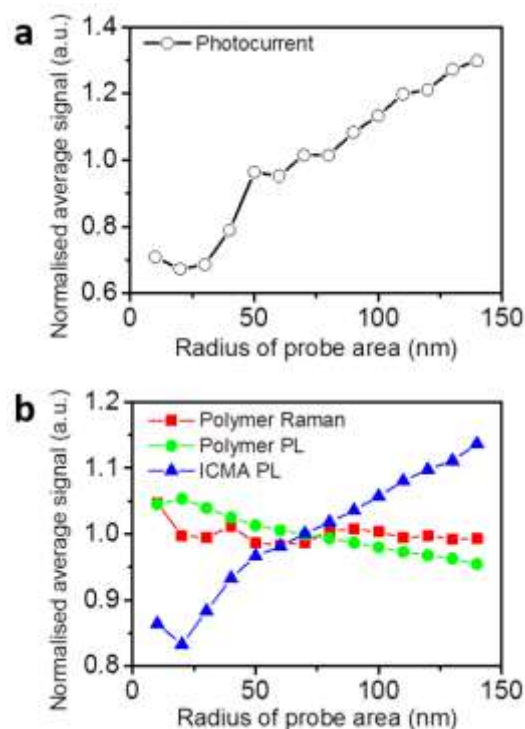

Fig. 5 Average (per pixel) (a) photocurrent, (b) intensity of polymer Raman (red squares), polymer PL (green circles) and fullerene PL (blue triangles) signals calculated in circular areas inside the white circle marked in Fig. 3e, as a function of radius increasing from 10 - 150 nm in the direction of the arrow. Radius step size: 10 nm. The average per pixel data in each circular area (radius: 10 – 150 nm) is normalised by the mean value for the entire circle area (radius: 150 nm) for easier comparison of trends.

molecules over these length-scales. However, as the size of probe area increases, average photocurrent and fullerene PL signal per pixel strongly increase while the average polymer PL signal per pixel slightly decreases. In fact, a similar trend for the photocurrent is observed over probe areas with radii of several hundreds of nanometres, eventually reaching saturation as the radius approaches 1 µm as shown in Supplementary Fig. S14. At such large length-scales the spatially-resolved device performance begins to resemble that of the macroscopic solar cell. The area-averaged photocurrent as a function of the size of probe area within the circle marked in Fig. 3e should be constant if the photocurrent generation efficiency were homogeneous at the tens of nanometre scale within the active layer. However, as shown in Fig. 5 this is clearly not the case. The strong dependence of photocurrent on probe area indicates strong local variations in photocurrent generation efficiency in the blend film, which is supported by the observation of small photocurrent hotspots outside the islands. The increase in fullerene PL with constant polymer Raman intensity indicates a change in local subsurface morphology as the probe area samples a more fullerene-rich domain, similar to that observed inside the topographic island in Fig. 3b. These results indicate that the local composition of the current
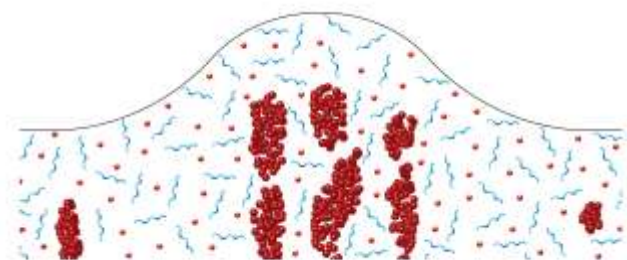
Fig. 6 Schematic diagram showing the proposed composition of the C8SiIDT-BT:ICMA blend surface. Relative distribution of fullerene and polymer molecules is shown at the surface and subsurface around a topographic island on the C8SiIDT-BT:ICMA blend including two photocurrent hotspots as revealed by simultaneous topographic, spectroscopic and electrical mapping results shown in Fig. 3.

hotspots is similar to that found inside the islands and that the local current variations are indeed real. This points to a hierarchical three-dimensional nanostructure in this blend containing small areas with optimal morphology (topographic islands and current hotspots) for efficient photocurrent generation and collection dispersed within a background with poor efficiency. The average photocurrent inside the good areas (current hotspots or islands) was found to be 1.5 - 2.3 times higher than the overall average photocurrent, indicating a substantial potential for improvement in short-circuit current (J_{sc}) if a similarly optimised morphology of sub-surface fullerene aggregates with nanoscale interspersion of polymer molecules can be obtained uniformly throughout the solar cell blend. Indeed, we observe a factor of two improvement in J_{sc} in pristine C8SiIDT-BT:PC$_{61}$BM (1:1) solar cell devices that consists of an optimised mixed morphology present throughout the blend, while the fill factor and open-circuit voltage remained the same as for the ICMA blend. See Supplementary Note 1 for comparison of the macroscopic performance between pristine C8SiIDT-BT:ICMA and pristine and annealed C8SiIDT-BT:PC$_{61}$BM solar cell devices.

Based on the STEOM results, we propose a schematic morphological description of the top surface of the C8SiIDT-BT:ICMA active layer shown in Fig. 6. The cross-sectional scheme shows the distribution of polymer and fullerene molecules at the surface and the sub-surface around an island and two current hotspots at each side of the island. Whilst composition is uniform along the surface skin, the subsurface region contains localised larger aggregates rich in fullerene surrounded by polymer molecules that lead to better charge collection and increased photocurrent. A somewhat similar fullerene aggregate wrapped in polymer skin morphology was reported previously using cross-sectional SEM[24], however a direct identification of chemical composition could not be possible in that study.

4. Conclusions

In this work, we have demonstrated a novel multi-parameter measurement method that allows non-destructive and simultaneous mapping of local morphology, chemical composition, optical and electrical properties of operating OPV devices with < 20 nm spatial resolution. We have shown that the complementary information and depth of resolution of TER and TEPL signals can provide surface and subsurface information, allowing a better understanding of the distribution of donor and acceptor molecules and their relationship to photocurrent generation and collection. Currently, such detailed insights into the interplay of surface morphology, chemical composition and photocurrent generation at the nanoscale cannot be directly obtained by any other analytical technique including far-field measurement methods (see Supplementary Note 8 for more details).

Moreover, we have applied this multiparameter mapping method to operating C8SiIDT-BT:ICMA and C8SiIDT-BT:PC$_{61}$BM blend (Supplementary Note 7) solar cells and demonstrated a direct correlation of local blend composition with optoelectronic properties. The simultaneous topographic, spectroscopic and electrical measurements revealed a hierarchical blend nanostructure in C8SiIDT-BT:ICMA solar cell blends with a combination of nanoscale photocurrent hotspots and larger islands of high efficiency and optimised blend ratio dispersed in a low efficiency blend background. We showed that in these blends ICMA molecules form impure subsurface aggregates containing a small amount of polymer molecules, which lead to local increase of measured photocurrent. This is contrary to the typically observed large aggregates of relatively pure PC$_{61}$BM in annealed C8SiIDT-BT:PC$_{61}$BM solar cell blends that lead to local reduction of photocurrent[14, 24], therefore requiring a different device optimisation strategy (Supplementary Note 7). It should be noted that macroscopic device data presented in Supplementary Note 1 cannot distinguish between these microscopic effects in pristine C8SiIDT-BT:ICMA and annealed C8SiIDT-BT:PC$_{61}$BM solar cell devices as both lead to a similar reduction of the macroscopic J_{sc} compared to pristine C8SiIDT-BT:PC$_{61}$BM solar cell device. However, we have shown that the nanoscale multi-parameter measurements on both C8SiIDT BT:ICMA and C8SiIDT BT:PC61BM solar cell devices are consistent with and can successfully explain the macroscopic device performance, validating the capability of STEOM to directly correlate macroscopic performance in OPV devices with nanoscale characteristics.

Furthermore, the multi-parameter measurement approach demonstrated here allows combination of almost any electrical AFM mode with spectroscopic measurements and therefore is expected to pave the way for the development of a multitude of new nanoscale characterisation capabilities to directly probe the effect of nanoscale materials, molecules and impurities on different electrical properties for e.g. surface potential, impedance etc. We expect that the detailed information that can be obtained from such multi-parameter measurements will play a significant role in guiding the rational design of a range of nanomaterial-based optoelectronic devices.

Acknowledgements

Notes and references

1. N. P. Dasgupta, J. Sun, C. Liu, S. Brittman, S. C. Andrews, J. Lim, H. Gao, R. Yan and P. Yang, *Adv. Mater.*, 2014, **26**, 2137-2184.
2. F. Bonaccorso, L. Colombo, G. Yu, M. Stoller, V. Tozzini, A. C. Ferrari, R. S. Ruoff and V. Pellegrini, *Science*, 2015, **347**, 1246501.
3. Z. Liu, J. Xu, D. Chen and G. Shen, *Chemical Society Reviews*, 2015, **44**, 161-192.
4. A. C. Atre, B. J. Brenny, T. Coenen, A. García-Etxarri, A. Polman and J. A. Dionne, *Nat. Nanotechnol.*, 2015, **10**, 429-436.
5. D. C. Coffey, O. G. Reid, D. B. Rodovsky, G. P. Bartholomew and D. S. Ginger, *Nano Lett.*, 2007, **7**, 738-744.
6. W. C. Tsoi, P. G. Nicholson, J. S. Kim, D. Roy, T. L. Burnett, C. E. Murphy, J. Nelson, D. D. C. Bradley, J.-S. Kim and F. A. Castro, *Energy Environ. Sci.*, 2011, **4**, 3646-3651.
7. J. C. Blakesley and F. A. Castro, *Phys. Rev. B.*, 2015, **91**, 144202.
8. N. Mauser and A. Hartschuh, *Chem. Soc. Rev.*, 2014, **43**, 1248-1262.
9. C. Blum, L. Opilik, J. M. Atkin, K. Braun, S. B. Kammer, V. Kravtsov, N. Kumar, S. Lemeshko, J. F. Li, K. Luszcz, T. Maleki, A. J. Meixner, S. Minne, M. B. Raschke, B. Ren, J. Rogalski, D. Roy, B. Stephanidis, X. Wang, D. Zhang, J. H. Zhong and R. Zenobi, *J. Raman Spectrosc.*, 2014, **45**, 22-31.
10. N. Kumar, S. Mignuzzi, W. Su and D. Roy, *EPJ Tech. Instrum.*, 2015, **2**, 9.
11. N. Kumar, B. Stephanidis, R. Zenobi, A. Wain and D. Roy, *Nanoscale*, 2015, **7**, 7133-7137.
12. T. Hartman, C. S. Wondergem, N. Kumar, A. van den Berg and B. M. Weckhuysen, *The journal of physical chemistry letters*, 2016, **7**, 1570-1584.
13. N. Lee, R. D. Hartschuh, D. Mehtani, A. Kisliuk, J. F. Maguire, M. Green, M. D. Foster and A. P. Sokolov, *J. Raman Spectrosc.*, 2007, **38**, 789-796.
14. X. Wang, D. Zhang, K. Braun, H. J. Egelhaaf, C. J. Brabec and A. J. Meixner, *Adv. Funct. Mater.*, 2010, **20**, 492-499.
15. S. Mignuzzi, N. Kumar, B. Brennan, I. S. Gilmore, D. Richards, A. J. Pollard and D. Roy, *Nanoscale*, 2015, **7**, 19413-19418.
16. A. J. Pollard, N. Kumar, A. Rae, S. Mignuzzi, W. Su and D. Roy, *J. Mater. Nanosci.*, 2014, **1**, 39-49.
17. W. Su, N. Kumar, N. Dai and D. Roy, *Chem. Commun.*, 2016.
18. W. Su, N. Kumar, S. Mignuzzi, J. Crain and D. Roy, *Nanoscale*, 2016, **8**, 10564-10569.
19. W. Su, N. Kumar, S. J. Spencer, N. Dai and D. Roy, *Nano Res.*, 2015, **8**, 3878-3886.
20. E. A. Pozzi, M. D. Sonntag, N. Jiang, J. M. Klingsporn, M. C. Hersam and R. P. Van Duyne, *ACS nano*, 2013, **7**, 885-888.
21. R. Zhang, Y. Zhang, Z. C. Dong, S. Jiang, C. Zhang, L. G. Chen, L. Zhang, Y. Liao, J. Aizpurua, Y. Luo, J. L. Yang and J. G. Hou, *Nature*, 2013, **498**, 82-86.
22. P. G. Nicholson and F. A. Castro, *Nanotechnology*, 2010, **21**, 26.
23. Y. H. Liu, J. B. Zhao, Z. K. Li, C. Mu, W. Ma, H. W. Hu, K. Jiang, H. R. Lin, H. Ade and H. Yan, *Nat. Commun.*, 2014, **5**, 8.
24. H. Hoppe, M. Niggemann, C. Winder, J. Kraut, R. Hiesgen, A. Hinsch, D. Meissner and N. S. Sariciftci, *Adv. Funct. Mater.*, 2004, **14**, 1005-1011.
25. K. Maturová, S. Van Bavel, M. Wienk, R. Janssen and M. Kemerink, *Nano Lett.*, 2009, **9**, 3032-3037.
26. M. Morana, H. Azimi, G. Dennler, H.-J. Egelhaaf, M. Scharber, K. Forberich, J. Hauch, R. Gaudiana, D. Waller, Z. Zhu, K. Hingerl, S. S. van Bavel, J. Loos and C. J. Brabec, *Adv. Funct. Mater.*, 2010, **20**, 1180-1188.
27. B. A. Collins, E. Gann, L. Guignard, X. He, C. R. McNeill and H. Ade, *J. Phys. Chem. Lett.*, 2010, **1**, 3160-3166.
28. P. E. Keivanidis, T. M. Clarke, S. Lilliu, T. Agostinelli, J. E. Macdonald, J. R. Durrant, D. D. Bradley and J. Nelson, *The Journal of Physical Chemistry Letters*, 2010, **1**, 734-738.
29. C. Müller, T. A. Ferenczi, M. Campoy-Quiles, J. M. Frost, D. D. Bradley, P. Smith, N. Stingelin-Stutzmann and J. Nelson, *Adv. Mater.*, 2008, **20**, 3510-3515.
30. J. Peet, J. Y. Kim, N. E. Coates, W. L. Ma, D. Moses, A. J. Heeger and G. C. Bazan, *Nat. Mater.*, 2007, **6**, 497-500.
31. A. Arias, J. MacKenzie, R. Stevenson, J. Halls, M. Inbasekaran, E. Woo, D. Richards and R. Friend, *Macromolecules*, 2001, **34**, 6005-6013.
32. R. Hansson, L. K. Ericsson, N. P. Holmes, J. Rysz, A. Opitz, M. Campoy-Quiles, E. Wang, M. G. Barr, A. D. Kilcoyne and X. Zhou, *J. Mater. Chem. A*, 2015, **3**, 6970-6979.
33. Y. Moritomo, T. Yasuda, K. Yonezawa, T. Sakurai, Y. Takeichi, H. Suga, Y. Takahashi, N. Inami, K. Mase and K. Ono, *Sci. Rep.*, 2015, **5**, 5.
34. B. A. Collins, Z. Li, C. R. McNeill and H. Ade, *Macromolecules*, 2011, **44**, 9747-9751.
35. L. S. Pingree, O. G. Reid and D. S. Ginger, *Adv. Mater.*, 2009, **21**, 19-28.
36. N. Kumar, S. J. Spencer, D. Imbraguglio, A. M. Rossi, A. J. Wain, B. M. Weckhuysen and D. Roy, *Physical Chemistry Chemical Physics*, 2016, **18**, 13710-13716.
37. M. A. Faist, Imperial College London, 2012.
38. J. K. J. van Duren, X. N. Yang, J. Loos, C. W. T. Bulle-Lieuwma, A. B. Sieval, J. C. Hummelen and R. A. J. Janssen, *Adv. Funct. Mater.*, 2004, **14**, 425-434.
39. A. M. Ballantyne, T. A. Ferenczi, M. Campoy-Quiles, T. M. Clarke, A. Maurano, K. H. Wong, W. Zhang, N. Stingelin-Stutzmann, J.-S. Kim and D. D. Bradley, *Macromolecules*, 2010, **43**, 1169-1174.
40. A. Hartschuh, *Angew. Chem. Int. Ed.*, 2008, **47**, 8178-8191.
41. B. Pettinger, K. F. Domke, D. Zhang, G. Picardi and R. Schuster, *Surf. Sci.* , 2009, **603**, 1335-1341.
42. T. Ichimura, S. Fujii, P. Verma, T. Yano, Y. Inouye and S. Kawata, *Phys. Rev. Lett.*, 2009, **102**, 186101.